Check for updates

Metal–organic framework/Nb₄C₃Tₓ MXene composites for ultrasensitive detection of dopamine†

Purna K. Boruah,[a] Nidhi Sharma,[bc] Manash R. Das, [ID] [bc] Ryo Ohtani, [ID] [a] Benjamin Le Ouay [ID] *[a] and Masaaki Ohba [ID] *[a]

An easy, *in situ* growth approach led to the formation of several composites of metal–organic frameworks and Nb₄C₃Tₓ MXenes mixed intimately at the submicron scale. The high affinity of MXene surface for dopamine, enhanced by a nanostructuration induced by MOFs, resulted in superior sensing performances. The system exhibited good linearity over the 1–100 nM range, with an excellent limit of detection of 0.2 nM.

Discovered in 2011, MXenes constitute an emerging class of 2D materials made from transition metal carbides or nitrides that possess high electrical conductivity, tuneable structures, and superior mechanical strength.[1–3] The general formula for MXene is $M_{n+1}X_nT_x$ (n = 1–3), where M represents an early transition metal (such as Ti, Mo or Nb), X represents carbon or nitrogen and T denotes surface termination groups (–OH, –O and –F).[4] The surface termination groups on the 2D ultrathin MXene nanosheets enable easy adsorption of cationic ions through electrostatic interactions. This combination of properties has made MXene-based materials extremely promising for various electrochemical applications, including sensing and biomedical applications.[5,6] Among the group of MXenes, Nb-based MXenes have been considerably less studied than Ti-based MXenes, likely because of a more difficult delamination for thicker monolayers.[7] Nb₄C₃Tₓ based-material applications in the electrochemical sensing field are still largely unexplored, despite a higher conductivity (1024 S cm⁻¹) compared to the extensively studied Ti₃C₂Tₓ (850 S cm⁻¹).[8] It is worth noting that MXenes can allow swift electron transport towards electrochemically active sites, thus promoting electrochemical

reactions.[9] MXenes have been used in biosensing without affecting biological molecules due to their excellent biocompatibility and affinity for biomolecules.[10]

Dopamine (DA) is a significant electrochemically active molecule with a high affinity for MXene surfaces[11] that commonly exists in the human body. It is a primary catecholamine molecule with a basal concentration ranging from 0.01–1 μM and is involved in many physiological and pathological aspects.[12] DA is a neurotransmitter that plays a crucial role in several biological processes, and abnormalities in DA levels can cause neuroendocrine disorders like Parkinson's and schizophrenia, as well as tardive dyskinesia.[13] Therefore, it is of great importance to developing selective and ultrasensitive methods for detecting DA, as it has significant analytical and diagnostic applications.

Detection of DA is typically done using enzyme-linked immunosorbent assay (ELISA) and high-performance liquid chromatography (HPLC).[14,15] Despite the sensitivity of these methods, they are also expensive, difficult to handle, time-consuming, and require highly skilled personnel to operate. Electrochemical detection techniques are a useful set of tools for overcoming these limitations and detecting different compounds with high precision and sensitivity.[16] By utilizing comparatively inexpensive potentiostats, it is possible to create transportable sensing devices, thereby enabling widespread access and even on-site detection.[17] However, electrochemical detection of DA poses a challenge in selective detection due to interference from uric acid (UA) and ascorbic acid (AA) because of their redox potentials being close to that of DA. To overcome this obstacle, the electrode must be chemically modified with a material that has high selectivity towards DA. MXene-based electrodes appeared as promising electrocatalytic systems for detecting DA, even in the presence of interfering species.[18] However, like other 2D layered materials, the spontaneous stacking of the MXene monolayers during electrode fabrication often leads to limited access to their surface, resulting in a significant decrease of their overall performances and sensitivities.

[a] *Department of Chemistry, Faculty of Science, Kyushu University, 744 Motooka, Nishi-ku, Fukuoka 819-0395, Japan. E-mail: leouay.benjamin@chem.kyushu-univ.jp, ohba@chem.kyushu-univ.jp*

[b] *Materials Sciences and Technology Division, CSIR-North East Institute of Science and Technology, Jorhat 785006, Assam, India*

[c] *Academy of Scientific and Innovative Research (AcSIR), Ghaziabad 201002, India*

† Electronic supplementary information (ESI) available. See DOI: https://doi.org/10.1039/d4cc00694a

Interfacing exfoliated MXene monolayers with porous materials such as metal–organic frameworks (MOFs) is a potent way to increase dramatically their performances. MOFs are a class of organic–inorganic hybrid materials with a highly porous structure and large surface area.[19] MOFs have found diverse applications in gas storage/separation, catalysis, energy storage, conversion, and sensing.[20–22] However, because the vast majority of MOFs are electronic insulators, the development of electrochemical systems based on pure MOFs has remained comparatively hampered.[23,24] To address these issues, one strategy is to interface MOFs with other functional materials (such as conductive polymers), resulting in composites that maintain a highly accessible porosity of their parent MOF, while introducing new properties.[25,26] Among these, MXene/MOF composites have emerged as a class of composites with high potential for applications.[19] For instance, Pang *et al.* recently demonstrated the use of MOFs as a way to greatly improve the performance of $Ti_3C_2T_x$ MXene layers in supercapacitors.[25]

In this article, we prepared delaminated $Nb_4C_3T_x$ layers and integrated them uniformly in composites with three-dimensional (3D) MOF networks. To the best of our knowledge, this work constitutes the first example of interfacing between Nb-based MXenes and MOFs. These 3D MOFs were crucial in preventing the re-stacking of $Nb_4C_3T_x$ nanosheets and providing a high accessibility towards their surface. The following composites were prepared by *in situ* growth of the corresponding MOFs in the presence of exfoliated $Nb_4C_3T_x$: $ZIF-67/Nb_4C_3T_x$, $MIL-100(Fe)/Nb_4C_3T_x$, $MIL-101(Fe)/Nb_4C_3T_x$ and $HKUST-1/Nb_4C_3T_x$. Also composites with ZIF-8 at four MOF-to-MXene ratios were achieved by varying the amount of MOF precursor (25%, 50% and 75% of the weight of the initial value of 100%), and referred to as $ZIF-8/Nb_4C_3T_x(25)$, $ZIF-8/Nb_4C_3T_x(50)$, $ZIF-8/Nb_4C_3T_x(75)$ and $ZIF-8/Nb_4C_3T_x(100)$. Detail on the nature of these composites is given in the ESI.† As a result, we optimized the distribution and size of the MOF particles on the $Nb_4C_3T_x$ sheets, which resulted in excellent performances for the selective and ultrasensitive electrochemical detection of DA. It is evident that this study introduces a new approach for designing and synthesizing $MOF/Nb_4C_3T_x$ composites with customizable structures and properties, enabling their applications in various electrochemical sensing.

Accordion-like $Nb_4C_3T_x$ (Fig. S1, ESI†) was prepared by selective etching of its parent Nb_4AlC_3 phase. $Nb_4C_3T_x$ was then exfoliated into single-layer sheets using high-energy probe ultrasonication (Scheme S1, ESI†). The morphology of the exfoliated $Nb_4C_3T_x$ was confirmed using SEM and HRTEM images. The SEM, TEM and HRTEM images clearly show the single-layer MXene sheets, as depicted in Fig. S2 (ESI†). Successful etching of the parent phase Nb_4AlC_3 was further confirmed by X-ray diffraction (Fig. S3, ESI†)[27] and Raman spectroscopy (Fig. S4, ESI†). In addition, $Nb_4C_3T_x$ presented numerous negatively charged surface termination groups (zeta potential: −33 mV, Fig. S5, ESI†), which promoted the adsorption of cations (Zn^{2+}, Co^{2+}, Fe^{3+} and Cu^{2+}), increasing the affinity of the MOFs for the $Nb_4C_3T_x$ nanosheets.[28] As a result, homogeneous composites of 3D MOFs with $Nb_4C_3T_x$ were obtained (detailed procedures are presented in the ESI† and in Scheme 1).
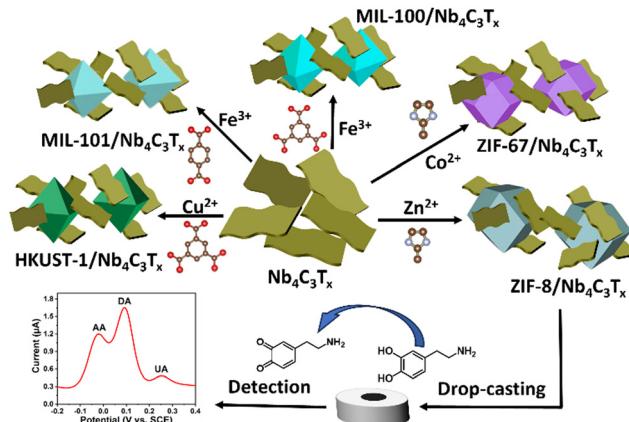
Scheme 1 Preparation of $MOF/Nb_4C_3T_x$ composites and detection of biomolecules.

The SEM and TEM imaging (Fig. 1) indicated that $ZIF-8/Nb_4C_3T_x(75)$ was composed of submicronic $Nb_4C_3T_x$ nanoflakes and MOF microcrystals, intimately mixed together at the microscale. The corresponding selected area electron diffraction (SAED) pattern (Fig. 1(c)) also confirmed the presence of monocrystalline $Nb_4C_3T_x$ sheets. The presence of Zn, C, N, Nb, O and F elements in $ZIF-8/Nb_4C_3T_x(75)$ has been confirmed and mapped through high-angle annular dark-field scanning transmission electron microscopy (HAADF-STEM) (Fig. 1(d)). Notably, this observation confirmed the intimate contact of $Nb_4C_3T_x$ with ZIF-8, with nanoflakes of the MXene (size: *ca.* 300 nm, indicated by red arrows in Fig. 1(d)) observed adhering to the surface of a ZIF-8 particle (size: *ca.* 1 μm). Composites' homogeneity with other MOFs was also confirmed by FESEM elemental mapping analysis (Fig. S17, ESI†).

At the macroscopic scale, the XRD pattern of various $ZIF-8/Nb_4C_3T_x(75)$ compositions confirms the presence of main peaks for both ZIF-8 and $Nb_4C_3T_x$ in the composites (Fig. 2(a)). In the XRD patterns of all other $MOF/Nb_4C_3T_x$ composites (Fig. S8–S11, ESI†), prominent diffraction peaks for the MOF and $Nb_4C_3T_x$ were also observed, indicating the successful preparation of the composites for all MOFs. The functional groups and surface functionalities of all MOFs and the composites were analyzed by
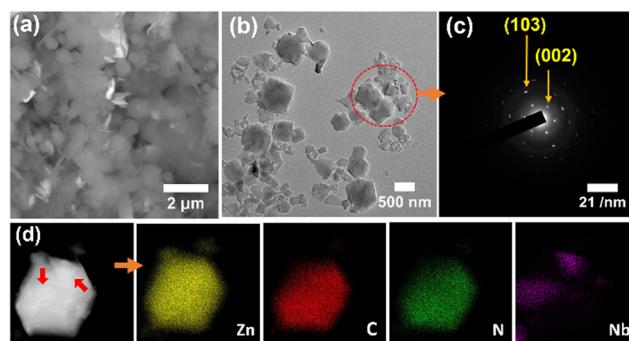
Fig. 1 (a)–(c) Observation of $ZIF-8/Nb_4C_3T_x(75)$ using SEM (a), TEM (b), and the corresponding SAED pattern (c). The indicated peaks correspond to the diffraction signal of $Nb_4C_3T_x$. (d) HAADF-STEM image and elemental mapping of $ZIF-8/Nb_4C_3T_x(75)$.
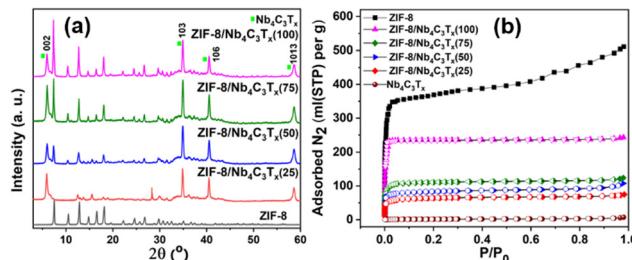
Fig. 2 (a) XRD pattern of various ZIF-8/Nb$_4$C$_3$T$_x$ composites. (b) N$_2$ adsorption isotherms of ZIF-8, Nb$_4$C$_3$T$_x$ and their composites (the closed symbols represent adsorption, while the open symbols represent desorption).

FT-IR spectroscopy analysis (details are discussed in ESI,† Fig. S12–S16). The X-ray photoelectron spectroscopy (XPS) survey spectrum of ZIF-8/Nb$_4$C$_3$T$_x$(75) displayed peaks attributed to Nb, C, N, O, and F elements (Fig. S19a, ESI†), consistent with the elemental mapping results. High-resolution XPS spectra of the Nb3d and Zn2p regions of ZIF-8/Nb$_4$C$_3$T$_x$(75) were consistent with previous reports of Nb$_4$C$_3$T$_x$[29] and ZIF-8 structures.[30] Similarly, XPS analysis of the relevant elements for all MOF/Nb$_4$C$_3$T$_x$ composites, were discussed in Fig. S18–S23 (ESI†).

Furthermore, both the MOF and MXene were confirmed to be present in the composites *via* TGA (Fig. S24a and b, ESI†) and SEM-EDX elemental analysis (Fig. S25–S32, ESI†), revealing their different compositions, and the modulation of the ZIF-8 content in the composites increases from ZIF-8/Nb$_4$C$_3$T$_x$(25) to ZIF-8/Nb$_4$C$_3$T$_x$(100). Finally, the specific surface area of all synthesized materials was measured using N$_2$ adsorption isotherms (Fig. 2(b), Fig. S33 and Table S2, ESI†). Bare Nb$_4$C$_3$T$_x$ lacks accessible porosity and has thus a specific surface area of 5 m^2 g^{-1} because of layer restacking. By incorporating MOF as a spacer, the porosity of the composites was increased markedly (Table S2, ESI†). Notably, the specific surface area of the composites ZIF-8/Nb$_4$C$_3$T$_x$(25) to ZIF-8/Nb$_4$C$_3$T$_x$(100) increased gradually with the ZIF-8 content. Interpolation of the increase trend to low ZIF-8 contents suggests a texturation of the Nb$_4$C$_3$T$_x$ by the presence of ZIF-8 (Fig. S34, ESI†), with a surface area specific to the MXene around 70 m^2 g^{-1}.

The electrochemical performance of the MOF/Nb$_4$C$_3$T$_x$ composites was investigated by drop-casting solids onto a 3 mm glassy carbon electrode (GCE) (details are presented in the ESI†). Electrochemical impedance spectroscopy (EIS) was used to investigate the charge transport properties of the modified electrodes. The interface charge transfer resistance (R_{ct}) values for different MOF/Nb$_4$C$_3$T$_x$ composites were measured by fitting with the Randles equivalent circuit.[31] The R_{ct} values for ZIF-8/Nb$_4$C$_3$T$_x$(75), ZIF-67/Nb$_4$C$_3$T$_x$, MIL-100/Nb$_4$C$_3$T$_x$, MIL-101/Nb$_4$C$_3$T$_x$, and HKUST-1/Nb$_4$C$_3$T$_x$ were 790, 908, 1026, 1065 and 1532 Ω, respectively (Fig. 3(a)). The R_{ct} values for all the composites were significantly lower than that of the bare GCE (5686 Ω, Fig. S35, ESI†). This suggests a higher rate of electron transfer and electrocatalytic activity for all composites. Among all the composites, ZIF-8/Nb$_4$C$_3$T$_x$(75) had the lowest R_{ct} value, making it the best system for sensing experiments.

To investigate the electrochemical biosensing activity of the composite materials towards DA, cyclic voltammetry (CV)
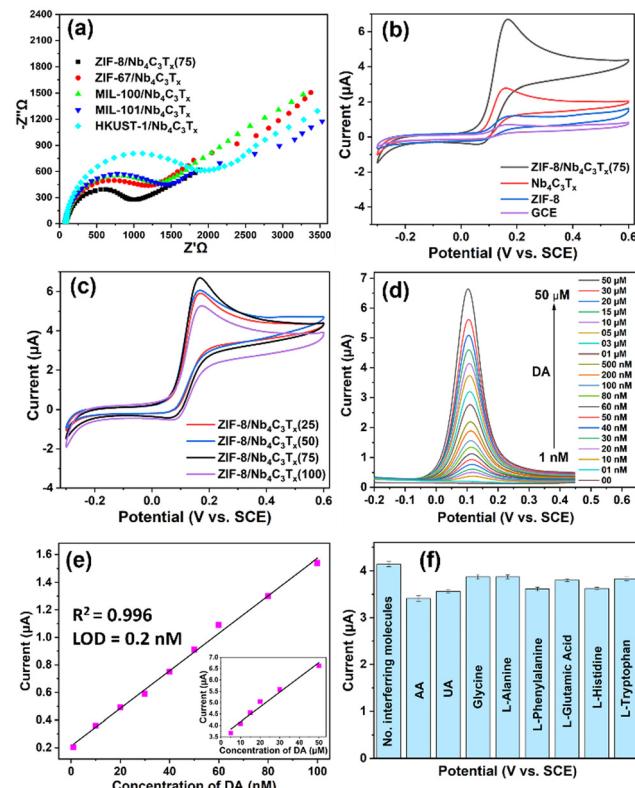

Fig. 3 (a) Nyquist plots of several MOF/Nb$_4$C$_3$T$_x$ electrodes. (b) and (c) Comparison of the CV responses of ZIF-8/Nb$_4$C$_3$T$_x$(75) and its constituents (b) and of ZIF-8/Nb$_4$C$_3$T$_x$ with different ZIF-8 contents (c), in the presence of 50 µM DA (20 mM HEPES buffer, pH 7, 0.1 M KCl and scan rate: 50 mV s^{-1}). (d) DPV responses of ZIF-8/Nb$_4$C$_3$T$_x$(75) in 20 mM HEPES buffer solution with different concentrations of DA and (e) corresponding plot of DPV peak current *vs.* concentration of DA and (f) Selectivity of ZIF-8/Nb$_4$C$_3$T$_x$(75) for DA detection in the presence of several interfering molecules (10 µM of each).

experiments were conducted using a ZIF-8/Nb$_4$C$_3$T$_x$ modified electrode in the presence and absence of DA. The results were compared to those of bare GCE, ZIF-8, and Nb$_4$C$_3$T$_x$ (Fig. 3(b)). The oxidation potential of 0.15 V was clearly defined, and the peak current was higher for ZIF-8/Nb$_4$C$_3$T$_x$(75). The peak corresponds to the oxidation of DA to dopamine-*o*-quinone through a two-electron transfer process (Scheme 1). The electrochemical responses of the other composites were also investigated (Fig. S36b, ESI†). The ZIF-8/Nb$_4$C$_3$T$_x$(75) composite exhibited a significantly higher peak current than the other composites, which can be attributed to its superior electron transfer rate. Moreover, the CV response of samples in the ZIF-8/Nb$_4$C$_3$T$_x$ series was compared (Fig. 3(c)). Increasing the MOF content in the composites leads to an increase in peak current up to ZIF-8/Nb$_4$C$_3$T$_x$(75), followed by a decrease due to excess MOF content in ZIF-8/Nb$_4$C$_3$T$_x$(100) as the more non-conductive MOF hinders electron transfer ability in the composite. The porosity of the composites plays a significant role in the adsorption of DA, but only to a certain extent. Beyond that, the electron transfer ability of the composites and their interaction with the MOF become crucial parameters for detecting DA. Furthermore, the π–π interaction between DA and MOF and –OH groups of

$Nb_4C_3T_x$ facilitate DA adsorption on the composite surface.[31] The stability of ZIF-8/$Nb_4C_3T_x$/GCE was tested by storing it in HEPES buffer for 20 days at 5 °C. The electrochemical response of DA was reduced by only 8% of the initial response value, indicating high stability in these conditions (Fig. S37, ESI†).

Differential pulse voltammetry (DPV) was adopted to improve the sensitivity by eliminating non-faradaic current, resulting in a stronger analytical signal compared to CV.[32] Fig. 3(d) illustrates the DPV responses of the ZIF-8/$Nb_4C_3T_x$(75) electrode in HEPES buffer solution in the presence of various concentrations of DA (ranging from 1 nM to 50 μM). The distinct oxidation potential of DA was observed at 0.11 V, and the peak current of this oxidation gradually increased with an increase in the concentration of DA from 1 nM to 50 μM. The DA oxidation peak is clearly visible even at a concentration of 1 nM (Fig. S38, ESI†). The calibration plot in Fig. 3(e) shows two domains where the peak current was linear to the DA concentration, denoting two distinct mechanisms at different concentration ranges. One domain ranged from 1 to 100 nM (slope: 13.6 μA μM^{-1}), and the other ranged from 5 to 50 μM (inset in Fig. 3(e); slope: 0.065 μA μM^{-1}). These two domains are likely related to the adsorption of DA onto $Nb_4C_3T_x$ or within the MOF near $Nb_4C_3T_x$, respectively. However, because the current ranges and concentration domains for either of these behaviours were well distinct, the system was suitable to analyze either of the domains with a good precision. We then focused on the low concentration domain (1–100 nM, Fig. S38, ESI†). The limit of detection (LOD) is calculated for a linear range of 1–100 nM using the 3σ method and found to be 0.2 nM. The LOD is significantly lower as compared to most of the previously reported MXenes and their composite materials (Table S3, ESI†).

The selectivity of the designed sensor was studied in the presence of high concentrations (10 μM) of various interferent molecules that are commonly present in our human body (Fig. 3(f)). Ascorbic acid (AA) and uric acid (UA) only showed a minor interference effect for the detection of DA due to the oxidation peak potential being close to DA. The distinct oxidation peaks were also observed for AA and UA in the presence of DA, and easily separated by peak deconvolution (Fig. S39, ESI†). Therefore, the designed sensor can simultaneously detect DA, AA and UA with excellent selectivity.

In summary, a simple *in situ* synthesis approach for the growth of various MOFs on $Nb_4C_3T_x$ MXene sheets was developed. The metal cations interact with negatively charged termination groups on $Nb_4C_3T_x$ sheets, facilitating the growth of MOF particles on $Nb_4C_3T_x$ sheets. The MOF plays a crucial role in increasing porosity, while the MXene provides conductivity to the composites. The composites obtained are highly porous and have superior electrolytic activity with a high electron transfer rate. The composites of MOF/$Nb_4C_3T_x$ and notably composites with ZIF-8 exhibited exceptional activity in selectively detecting small biomolecules such as dopamine. This highlights their potential for developing ultrasensitive electrochemical sensors for the detection of various organic and inorganic molecules.

Conflicts of interest

There are no conflicts to declare.

Notes and references

1 M. Naguib, M. Kurtoglu, V. Presser, J. Lu, J. Niu, M. Heon, L. Hultman, Y. Gogotsi and M. W. Barsoum, *Adv. Mater.*, 2011, **23**, 4248–4253.
2 D. H. Ho, Y. Y. Choi, S. B. Jo, J.-M. Myoung and J. H. Cho, *Adv. Mater.*, 2021, **33**, 2005846.
3 J. Pang, R. G. Mendes, A. Bachmatiuk, L. Zhao, H. Q. Ta, T. Gemming, H. Liu, Z. Liu and M. H. Rummeli, *Chem. Soc. Rev.*, 2019, **48**, 72–133.
4 C. Liu, Y. Bai, J. Wang, Z. Qiu and H. Pang, *J. Mater. Chem. A*, 2021, **9**, 11201–11209.
5 S. J. Kim, H. J. Koh, C. E. Ren, O. Kwon, K. Maleski, S. Y. Cho, B. Anasori, C. K. Kim, Y. K. Choi, J. Kim, Y. Gogotsi and H. T. Jung, *ACS Nano*, 2018, **12**, 986.
6 K. Huang, Z. Li, J. Lin, G. Han and P. Huang, *Chem. Soc. Rev.*, 2018, **47**, 5109.
7 S. Zhao, C. Chen, X. Zhao, X. Chu, F. Du, G. Chen, Y. Gogotsi, Y. Gao and Y. Dall'Agnese, *Adv. Funct. Mater.*, 2020, **30**, 2000815.
8 P. A. Rasheed, R. P. Pandey, F. Banat and S. W. Hasan, *Matter*, 2022, **5**, 546–572.
9 M. R. Lukatskaya, S. Kota, Z. Lin, M.-Q. Zhao, N. Shpigel, M. D. Levi, J. Halim, P.-L. Taberna, M. W. Barsoum, P. Simon and Y. Gogotsi, *Nat. Energy*, 2017, **2**, 17105.
10 F. Shahzad, A. Iqbal, H. Kim and C. Koo, *Adv. Mater.*, 2020, **32**, 2002159.
11 G. S. Lee, T. Yun, H. Kim, I. H. Kim, J. Choi, S. H. Lee, H. J. Lee, H. S. Hwang, J. G. Kim, D.-W. Kim, H. M. Lee, C. M. Koo and S. O. Kim, *ACS Nano*, 2020, **14**, 11722–11732.
12 J. Yang, Y. Hu and Y. C. Li, *Biosens. Bioelectron.*, 2019, **135**, 224–230.
13 B. Patella, A. Sortino, F. Mazzara, G. Aiello, G. Drago, C. Torino, A. Vilasi, A. O'Riordan and R. Inguanta, *Anal. Chim. Acta*, 2021, **1187**, 339124.
14 S. M. Namkung, J. S. Choi, J. H. Park, M. G. Yang, M. W. Lee and S. W. Kim, *Korean J. Clin. Lab. Sci.*, 2017, **49**, 220e226.
15 H.-X. Zhao, H. Mu, Y.-H. Bai, H. Yu and Y.-M. Hu, *J. Pharm. Anal.*, 2011, **1**, 208e212.
16 X. Xie, D. Ping Wang, C. Guo, Y. Liu, Q. Rao, F. Lou, Q. Li, Y. Dong, Q. Li, H. B. Yang and F. X. Hu, *Anal. Chem.*, 2021, **93**, 4916–4923.
17 K. Xie, J. Wang, S. Xu, W. Hao, L. Zhao, L. Huang and Z. Wei, *Mater. Des.*, 2023, **228**, 111867.
18 P. A. Rasheed, R. P. Pandey, T. Gomez, K. A. Jabbar, K. Prenger, M. Naguib, B. Aïssa and K. A. Mahmoud, *Electrochem. Commun.*, 2020, **119**, 106811.
19 H. Saini, N. Srinivasan, V. Šedajová, M. Majumder, D. P. Dubal, M. Otyepka, R. Zboril, N. Kurra, R. A. Fischer and K. Jayaramulu, *ACS Nano*, 2021, **15**, 18742–18776.
20 H. Li, K. Wang, Y. Sun, C. T. Lollar, J. Li and H. C. Zhou, *Mater. Today*, 2018, **21**, 108.
21 Y. B. Huang, J. Liang, X. S. Wang and R. Cao, *Chem. Soc. Rev.*, 2017, **46**, 126.
22 T. Ma, H. Li, J.-G. Ma and P. Cheng, *Dalton Trans.*, 2020, **49**, 17121–17129.
23 L. S. Xie, G. Skorupskii and M. Dincă, *Chem. Rev.*, 2020, **120**, 8536–8580.
24 Y. Xue, S. Zheng, H. Xue and H. Pang, *J. Mater. Chem. A*, 2019, **7**, 7301–7327.
25 C. Liu, Y. Bai, W. Li, F. Yang, G. Zhang and H. Pang, *Angew. Chem., Int. Ed.*, 2022, **61**, e202116282.
26 B. Le Ouay, M. Boudot, T. Kitao, T. Yanagida, S. Kitagawa and T. Uemura, *J. Am. Chem. Soc.*, 2016, **138**, 10088–10091.
27 Y. Tan, Z. Zhu, X. Zhang., J. Zhang, Y. Zhou, H. Li, H. Qin, Y. Bo and Z. Pan, *Int. J. Hydrogen Energy*, 2021, **46**, 1955–1966.
28 L. Ding, D. Xiao, Z. Lu, J. Deng, Y. Wei, J. Caro and H. Wang, *Angew. Chem., Int. Ed.*, 2020, **59**, 8720–8726.
29 S. S. Zhao, X. Meng, K. Zhu, F. Du, G. Chen, Y. J. Wei, Y. Gogotsi and Y. Gao, *Energy Storage Mater.*, 2017, **42e8**.
30 C. Liu, Y. Bai, J. Wang, Z. Qiu and H. Pang, *J. Mater. Chem. A*, 2021, **9**, 11201–11209.
31 D. Butler, D. Moore, N. R. Glavin, J. A. Robinson and A. Ebrahimi, *ACS Appl. Mater. Interfaces*, 2021, **13**, 11185–11194.
32 M. Hadi and A. Rouhollahi, *Anal. Chim. Acta*, 2012, **721**, 55–60.